

Computational Analysis of Ceramic Heat Exchangers for Supercritical CO₂ Brayton Cycle in CSP Applications at High-Temperatures

Dorri Jarrahbashi
Assistant Professor
Texas A&M University
College Station, TX

Sandeep R. Pidaparti
Graduate Student
Georgia Institute of Technology
Atlanta, GA

Taegy Kang
Graduate Student
Georgia Institute of Technology
Atlanta, GA

Devesh Ranjan
Associate Professor
Georgia Institute of Technology
Atlanta, GA

ABSTRACT

The maximum temperature at the turbine inlet is a key factor in determining the efficiency of conventional thermal to electric conversion cycles. Turbine inlet conditions are now limited to 550°C at 20 MPa due to degradation in the mechanical behavior of metal alloys at >600°C. Operation of heat exchangers (HEX) at temperatures greater than 750°C would enable a transformative increase in cycle efficiency from ~35% to ~50% for electrical energy conversion in concentrated solar power (CSP) systems. This outcome is aligned with the Department of Energy (DOE) Sunshot initiative for clean and affordable energy conversion with a pathway towards the 6¢/kWh target by 2020. A novel primary HEX made of a new metal-coated composite (cermet) for heat transfer between high-temperature (>750°C) molten salt as the heat transfer medium and super-critical carbon dioxide (SCO₂) as the working fluid has been designed for use in the SCO₂ Brayton cycle as the power block of CSP plants. A multi-region computational model implemented in open source computational fluid dynamics (CFD) code OpenFOAM has been deployed to study the thermal-hydraulic behavior of SCO₂ and molten salt inside the channels and conjugate heat transfer between the solid and fluid regions of the HEX. Fluid interpolation tables (FIT) libraries based on a piecewise biquintic spline interpolation of Helmholtz energy have been integrated with OpenFOAM to model SCO₂ properties. The objective of this study is to obtain the heat transfer capacity and pressure drop in the HEX. The threshold for the proposed design is a pressure drop less than 100 kPa on the SCO₂ side and power density greater than one MW/m³. Wide ranges of SCO₂ inlet conditions and different molten salts have been implemented into the model to detect the optimum operating conditions with the proposed design.

INTRODUCTION

In a Concentrated Solar Power (CSP) system, a thermal power cycle produces electricity utilizing solar energy. The disadvantage of solar-driven power cycle is the intermittent nature of the sun's radiation. To overcome this shortcoming, thermal storage using different storage mediums, e.g. molten salt, liquid metals, etc have been deployed to facilitate power production during the night and transfer heat to the working fluid. Molten salt may be used as both a heat transfer fluid (HTF) and a storage fluid in central receiver plants. Generally, the HTF is heated to 565°C in the receiver and then, flows through a HEX (HEX) to transfer the energy collected from the sun to the working fluid. Operating limits of CSP plants are dictated by the maximum operating temperature and high melting point of the HTF that impose a limit on the thermal efficiency of the plant and might lead to blockage in the receiver pipes. In order to defy solidification of molten salts at temperatures above ambient and avoid the potential blockage and damage to the HEXs and piping, solar receivers with fluid exit temperatures greater than 650°C and heat transfer fluids around 800°C temperatures are required. However, the maximum operating temperature of molten salt may impose serious restrictions. Furthermore, the cycle must be developed using high-temperature materials with high corrosion and oxidation resistance under long-term high-temperature conditions.

Using supercritical CO₂ (sCO₂) as the working fluid in closed Brayton cycle for thermal to electric energy conversion has applications in advanced nuclear reactors [1-3] and in concentrated solar power plants. A review of the applications of the sCO₂ Brayton cycle technology using various heat sources, e.g. nuclear, fossil fuel, and waste heat can be found in [4-8]. By using CO₂ near its critical point at the compressor inlet, the lower specific volume and augmented heat transfer reduce the back work ratio and enhance thermal to electric conversion efficiency. Furthermore, a more compact turbomachinery and HEX system compared to air Brayton cycles and superheated/supercritical steam Rankine cycles is expected which reduce the costs and the size of overall plant footprint. Evaluation of different power cycles, e.g. air Brayton cycle, steam Rankine cycle and sCO₂ Brayton cycle shows that sCO₂ power cycle is potentially the most efficient power cycle for high-temperature CSP applications [9, 10]. Turchi et al. [11-13] and Avila-Martin et al. [14] showed that sCO₂ recompression Brayton cycle provided higher cycle efficiency compared to the state-of-the-art supercritical or superheated steam cycles for a wide range of pressure ratios. A modular solar power tower (SPT) system with sCO₂ Brayton cycle has been proposed by Ma et al. [15]. At the high pressure of interest (>20 MPa), sCO₂ Brayton cycle operates in a single phase. As a result, it can efficiently exchange heat with sensible heat storage such as molten salt deployed in most CSP plants.

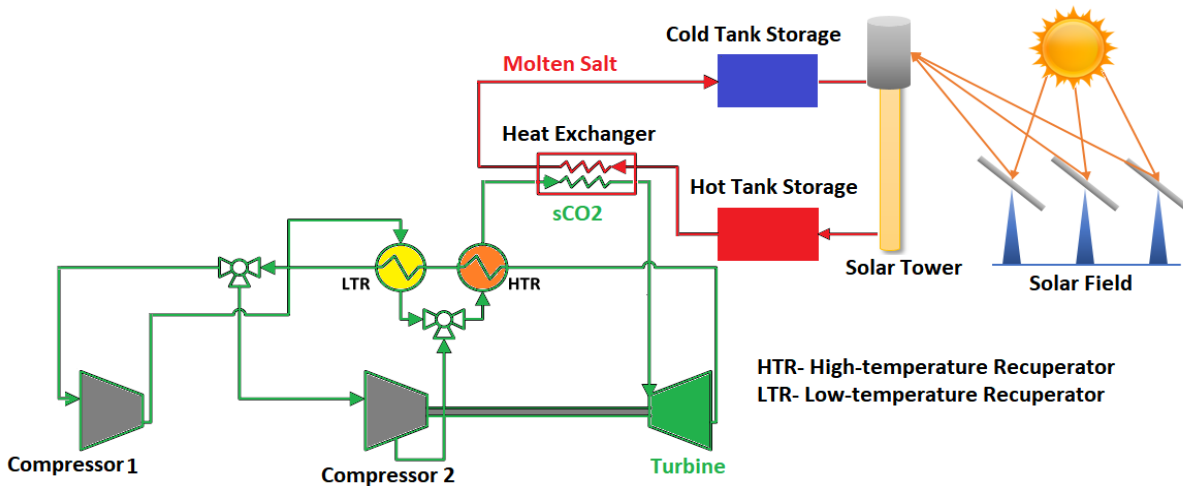


Figure 1. Schematic of a recompression sCO₂ power cycle integrated with the concentrated solar power plant.

Solar power tower system can be integrated with sCO₂ Brayton cycles via two approaches. In the first approach, sCO₂ works as both working fluid and heat transfer fluid [16, 17]. This method has the advantage of eliminating the HEX between the working and high-temperature fluids. However, designing the solar receiver and thermal storage for sCO₂ is very challenging [14, 18]. In the second approach, sCO₂ is used as the working fluid in the power cycle [19]. In this configuration shown schematically in Figure 1, the solar receiver uses another HTF, e.g. molten salt, liquid metal or thermal oil. This system consists of a heliostat field, a molten salt receiver, and a two-tank molten salt thermal storage coupled with sCO₂ Brayton cycle. Numerous recuperators are required to achieve the high thermal efficiencies expected from sCO₂ Brayton cycle. Molten salt is heated in the solar receiver from the sun's energy and CO₂ is heated through the primary aka main HEX. Numerical analysis of Wang et al. [19] showed that by increasing the molten salt temperature, the turbine inlet temperature increased and as a result, the overall cycle efficiency was enhanced. However, they demonstrated that by increasing the temperature of the hot molten salt, the exergy efficiency of the solar receiver increased initially and then decreased with further increase in the molten salt temperature. Thus, an optimum hot salt temperature within the allowable temperature range of the molten salt exists for each system. For instance, the maximum allowable temperature for solar salt (a mixture of 60 wt% NaNO₃ and 40 wt% KNO₃) is 565°C while the optimum theoretical temperature obtained by Wang et al. [19] is around 600°C. Their recommendation for the maximum allowable molten salt temperature for an integrated solar power tower and sCO₂ power cycle is 680°C. Increasing the temperature of the hot molten salt raises serious concerns about the maximum

allowable temperature of the materials implemented in building the primary HEX. Conventional and affordable metal alloys, e.g. Ni-based alloys and stainless steels used to build HEXs in such high-pressure/high-temperature SCO_2 systems and their strength reduction with temperature leads to an operating temperature limit at turbine inlet conditions ($\sim 650^\circ\text{C}$) at 20 MPa [4]. Employing higher-strength, high-temperature metal alloys to operate at $>750^\circ\text{C}$ in SCO_2 cycles is a promising way to increase the cycle efficiency.

This research is conducted as a part of “SunShot Concentrating Solar Power R&D” program initiated by the U.S. Department of Energy (DOE) in 2011. The purpose of this program is to promote technologies to provide lower electricity cost (6¢/kWh by 2020) and higher efficiency (more than 50%) for thermal to electric conversion compared to existing CSP plants. The SunShot target for CSP power tower for a turbine inlet temperature of 650°C requires high temperatures ($650\text{--}700^\circ\text{C}$) and pressures (20-25 MPa) in the solar receiver. The current maximum thermal storage temperature in a central tower receiver is 567°C [20]. This paper explores the advantages of replacing the existing HEX materials with ceramic composites (cermet) in building next generation of HEXs for higher temperature applications ($>750^\circ\text{C}$). Previous studies [15, 21] have investigated the possibility of reaching efficiencies $>50\%$ in SCO_2 Brayton cycle configurations with dry cooling, compatible with CSP applications via theoretical modeling. In their modeling approach, they assumed that the effectiveness of the HEXs and recuperators were 95% and the outlet temperature of the working fluid was set to the design conditions at the compressor and turbine inlets. In this paper, we focus on the computational modeling and design of microchannel ceramic HEXs working with molten salt and SCO_2 at higher temperatures using a novel cermet material that has the potential to withstand temperatures higher than 750°C . Printed circuit heat exchangers (PCHE) commercially manufactured by Heatric [29], have many advantages, e.g. low-pressure drop, high surface area, high effectiveness, and compactness. PCHEs allow a large pressure difference between the cold and hot side for SCO_2 Brayton cycle applications.

The properties of this special cermet developed at Purdue University [22, 23] at 800°C are outlined in Table 1. The cermet is resistant to corrosion under these conditions. Another advantage of this cermet is its thermal compatibility. The thermal expansion coefficients of ceramic and metal in this cermet differ by about 13% at 25°C ($4.0 \times 10^{-6}/^\circ\text{C}$ and $4.5 \times 10^{-6}/^\circ\text{C}$, respectively) and at temperatures up to 2700°C ($10.2 \times 10^{-6}/^\circ\text{C}$ and $9.2 \times 10^{-6}/^\circ\text{C}$, respectively). A wide range of initial conditions for the inlet temperature and mass flux of SCO_2 and potential molten salts for CSP applications will be evaluated. The design targets for the HEX design is heat transfer capacity and HEX effectiveness greater than one MW/m^3 and 90%, respectively. The other important design parameter is the pressure drop within the HEX that has been neglected in the past [11, 12]. In this paper, we will calculate the pressure drop in both fluids, i.e. SCO_2 and molten salt within the HEX and will show that their values are smaller than 100 kPa. The compactness, low-pressure drop, high-temperature resistance, and high heat transfer effectiveness of the microchannel ceramic HEX make them a very attractive choice for SCO_2 cycles integrated with CSP plants at high temperatures $>750^\circ\text{C}$.

Table 1. Thermophysical and mechanical properties of cermet at 800°C .	
Density (kg/m^3)	11400
Conductivity ($\text{W}/\text{m}\cdot\text{K}$)	65.9
Specific Heat ($\text{J}/\text{kg}\cdot\text{K}$)	285
Thermal Diffusivity (m^2/s)	0.2×10^{-4}
Thermal Expansion Coefficient ($1/\text{K}$)	6.39×10^{-6}
Young Modulus (GPa)	407

MOLTEN SALT PROPERTIES

Molten salts as heat transfer agents have been used in nuclear reactors in the Aircraft Reactor Experiment (ARE) and the Molten Salt Reactor Experiment (MSRE) programs [24]. One mega Watt Molten-Salt Electric Experiment (MSEE), the 2.5 MWe THEMIS and the 10 MWe solar two central receiver power plants were among the first concentrated solar power CSP plants that utilized molten salt as both the HTF and thermal storage medium [24]. The most important properties of molten salt are thermal instability at high temperature, low melting point, high boiling point, low vapor pressure, substantially less than one atmosphere at operating temperatures to avoid volatility, large heat capacity, large thermal conductivity, low viscosity, compatibility with HEX and piping material, low Prandtl number, stability under radiation, and low costs [25]. Molten salt purity and potentials for impurities to plug the channels pose

additional complexities to the molten salt use in HEXs. The main properties of the conventional molten salts and the experimental correlations of viscosity within temperature range of interest is given in Table 2 [26, 27]. Two prominent molten salts suitable for lower temperature applications (<600°C) are referred to as solar salt (a eutectic mixture of sodium nitrate, 60% and potassium nitrate, 40% by weight) and Hitec (a eutectic mixture of sodium nitrate, 7% and potassium nitrate, 53%, and Sodium nitrite 40% by weight). The maximum operating temperature for these two salts is 600°C and 553°C, respectively. Thus, for the high-efficiency SCO₂ Brayton cycle of interest, the upper temperature poses a limit. The high melting point of the eutectic nitrate salts necessitates the installation of trace heating in the field piping to prevent freezing and the installation of a cold trap to keep melting point low to remove impurities. These salt mixtures are suitable for central receiver plants with storage at the maximum temperature of 567°C.

Halide salts, e.g. fluoride salts and chloride salts are stable at a higher operating temperature range (700-900°C) and their melting temperature is lower than the nitrate and nitrite salt. LiF-BeF₂ (also known as FLiBe [67-33 mol%]), LiF-NaF-KF (also known as FLiNaK [46.5-11.5-42 mol%]), and KCl-MgCl₂ (67-33 mol%), are among the most attractive candidates under investigation at University of Wisconsin [24]. They all have a melting point lower than the nitrate and nitrite salt. FLiBe and FLiNaK have been recommended to be used as the primary and secondary coolant due to their high thermal stability for temperatures higher than 900°C in the AHTR (Advanced High-Temperature Reactor) concept with application in the nuclear fission field [28]. FLiNaK that has almost similar chemical properties as FLiBe, is a good replacement for Be salt due to its low toxicity and prominent heat transfer properties [26]. LiF-NaF-BeF₂ (FLiNaBe) is another nuclear salt usually with a composition of 0.31-0.31-0.38 mol%. It has a lower melting point compared with FLiNaK and FLiBe and higher than KCl-MgCl₂, solar salt and Hitec and higher density than FLiBe, Hitec, solar salt, KCl-MgCl₂. The density of FLiNaBe is very close to that of FLiNaK [26]. Comparing thermal conductivities shows that FLiBe, FLiNaK, and FLiNaBe rank first to third in decreasing order, respectively. KCl-MgCl₂ has a higher thermal conductivity compared with Hitec and solar salt yet smaller than the nuclear salts, i.e. FLiBe, FLiNaK, and FLiNaBe. In general, unlike the fluoroborates and Li-containing mixtures, magnesium chlorides are less expensive; however, they have lower heat transfer properties. For CSP applications, nitrogen-based salt mixtures are less expensive and less corrosive than chlorides and fluorides, while their thermal properties are inferior. The effects of molten salt on heat transfer in the microchannel ceramic heat exchanger will be discussed in this paper. One of the major goals of this study is to evaluate the capabilities of KCl-MgCl₂ in CSP application because this salt is less expensive yet has lower heat transfer capabilities compared to fluoride salts. KCl-MgCl₂ has a lower melting point and higher maximum applicable temperature compared to the conventional salts, i.e. Hitec and solar salts.

Table 2. Properties of common molten salts [28]

Salt Mixture	FLiBe	FLiNaK	FLiNaBe	KCl-MgCl ₂	Solar Salt	Hitec
Melting Point (K)	730	727	569	705	495	415
Maximum Temperature (K) [28, 29]	1073	1050	1025	1030	873	808
Density (kg/m ³)	2413	2579.3-0.624T	2435.8-0.45T	2007-0.4571T	2263.628-0.636T	2279.799-0.7324T
Temperature range for density correlation (K)	788-1094	933-1170	800-1025	1017-1174	573-873	448-773
Heat Capacity (J/kg.K)	2385	1880	2200	1155	1396.044+0.17T	1560
Thermal Conductivity (W/m.K)	1.10	0.85	0.70	0.55	0.45	0.48

COMPUTATIONAL METHOD & COMPARISON WITH EXPERIMENT

A coupled fluid flow and heat transfer solver for multi-regions implemented in OpenFOAM [32] software are used to simulate the transient fluid flow and heat transfer between the fluid and solid regions in the HEX. This code combines solid and fluid solvers to calculate the conjugate heat transfer. A transient and density-based compressible flow solver and the semi-implicit method for pressure-linked equations (SIMPLE) is used in the fluid regions. The density and pressure obtained from the former iteration are used to solve the pressure, correct the momentum velocities according to the new pressure field, and adjust the pressure level to obey overall mass continuity. The continuity, momentum, and energy equation are as follows.

$$\frac{\partial \rho}{\partial t} + \frac{\partial}{\partial x_j} (\rho u_j) = 0 \quad (1)$$

$$\frac{\partial \rho u_i}{\partial t} + \frac{\partial}{\partial x_j} [\rho u_i u_j + p \delta_{ij} - \tau_{ij}] = 0 \quad (2)$$

$$\frac{\partial \rho e_0}{\partial t} + \frac{\partial}{\partial x_j} [\rho e_0 u_j + u_j p + q_j - u_j \tau_{ij}] = 0 \quad (3)$$

$$e_0 = e + \frac{u_i u_i}{2} \quad (4)$$

where ρ , u , q , e_0 , τ , δ , p are the fluid density, velocity, heat transfer rate, total energy, shear stress, Kronecker delta, and pressure, respectively. The properties of CO₂ is provided by integrating FIT (Fluid Property Interpolation Tables) program into the CFD solver to close the system of equations. The properties of CO₂ required to solve the governing equations have been obtained by utilizing a modified version of biquintic spline interpolation of Helmholtz free energy and all its derivatives to accurately model the properties of CO₂. The standard k - ϵ turbulence model with enhanced wall treatment has been implemented.

$$\frac{\partial \rho k}{\partial t} + \frac{\partial}{\partial x_j} (\rho k u_j) = \frac{\partial}{\partial x_j} \left[\left(\mu + \frac{\mu_t}{\sigma_k} \right) \frac{\partial k}{\partial x_j} \right] + P_k + P_b - \rho \epsilon - Y_M + S_k \quad (5)$$

$$\frac{\partial \rho \epsilon}{\partial t} + \frac{\partial}{\partial x_j} (\rho \epsilon u_j) = \frac{\partial}{\partial x_j} \left[\left(\mu + \frac{\mu_t}{\sigma_k} \right) \frac{\partial \epsilon}{\partial x_j} \right] + \frac{C_{1\epsilon} \epsilon}{k} (P_k + C_{3\epsilon} P_b) - \frac{C_{2\epsilon} \rho \epsilon^2}{k} + S_\epsilon \quad (6)$$

where μ_t is the turbulent viscosity and S_k and S_ϵ are source terms. σ_k , σ_ϵ , C_μ , $C_{1\epsilon}$, $C_{2\epsilon}$, and $C_{3\epsilon}$ are model constants. P_k and P_ϵ are the production of kinetic energy and buoyancy terms, respectively. Y_M is the contribution of the fluctuating dilation in compressible turbulence to the overall dissipation rate. The same fluid solver (uncoupled from the solid solver) and the implemented FIT library were previously used by the authors in two different applications: (1) to study the two-phase behavior of SCO₂ very close to the critical point in a venturi nozzle [30] and (2) supercritical carbon dioxide flow in see-through labyrinth seals [31]. The results showed a very good agreement with the experiments at very rigorous conditions close to the critical point where the thermophysical properties of CO₂ vary drastically and the computational simulation is very challenging. For the conjugated heat transfer in HEX simulations, another solver is required to solve the Laplace equation for the conductive heat transfer in the solid region. Heat equation for the solid domain is as follows:

$$-\frac{\partial}{\partial x_j} \left(\kappa \frac{\partial T}{\partial x_j} \right) = 0 \quad (7)$$

where T is the temperature and κ is the thermal conductivity of the solid. The interface heat flux is then matched at the fluid/solid interface. The abovementioned conjugated heat transfer and flow solver is compared with the available experimental data for a highly efficient PCHE with application in advanced SCO₂ Brayton cycles [32].

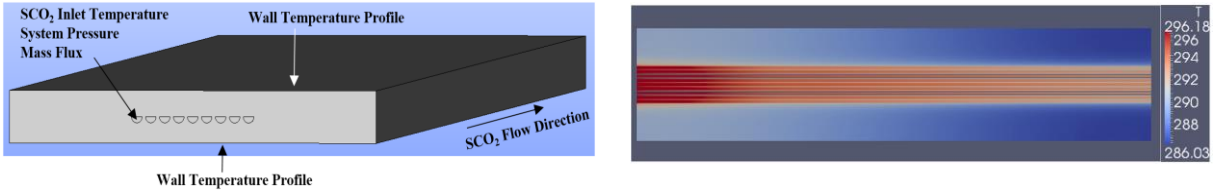


Figure 2. (Left) Geometry and boundary conditions of the modeled PCHE used for code validation (SCO₂ flows normal to the front wall, (right) steady-state temperature in Kelvin for both solid and fluid regions in the flow direction within the channels.

This HEX is made of stainless steel (SS316) and is consisted of nine parallel and straight semi-circular channels of 1.9 mm diameter with SCO₂ as the heat transfer medium investigated under cooling conditions (see Figure 2). The hydraulic diameter of the channels is 1.16 mm and the length of the HEX is 0.5 m. In that experiment, ten aluminum water blocks were installed on the top and bottom wall of the HEX for measuring the local heat removal by balancing the energy on each cooling block. The experimental wall temperatures obtained by Kruiuzenga et al. [32] for steady-state conditions (when the heat balance between water and CO₂ was less than 10%) are applied in the computational model. A fourth order polynomial curve fitted to the experimental wall temperature has been imposed as the boundary conditions on the top and bottom walls. The total mass flux of SCO₂ is set to 762 kg/m²s at the channel inlets. The inlet temperature and pressure of SCO₂ are set to 25°C and 7.5 MPa, respectively. To save the computational resources, the mesh inside and near the semicircular channels is set finer than that of the bottom and the top plates. The heat removed from SCO₂ by water can be calculated as $\dot{Q}_{CO_2} = GA(h_{in} - h_{out})$, where G, A, h_{in}, h_{out} are the mass flux, the surface area of the nine channels, and the fluid enthalpy at the inlet and outlet of the channels, respectively. The enthalpy is calculated based on the temperature and pressure at the inlet and outlet of the channels. Comparing the experimentally measured power removal with that of the current computational model for 7.5 MPa, 25°C, and 762 kg/m²s demonstrated a 10% error. The steady-state temperature contour for the nine-channel ceramic heat exchanger model in the spanwise direction within the channels is shown in Figure 2.

CERMET HEX FLOW CONFIGURATION

The design of the cermet HEXs is shown in Figure 3. The ceramic HEX will be formed by joining patterned (channeled) plates to mating (non-channeled) plates. Each patterned HEX plate will contain four 3 mm deep, 6 mm wide semi-circular channels, and 3 mm apart. The proposed ceramic HEX model is 10 cm wide, 15 cm long and 10 cm thick. In order to increase the heat transfer area per unit volume, a serpentine channel design is considered as shown in Figure 3. Inlet and outlet headers will be pressed into the plate to evenly distribute the fluid flows into the channels. The computational model consists of a rectangular box and three layers of semi-circular channels including the headers made of the cermet as Figure 3 shows. SCO₂ is introduced into two layers of channels shown in blue and molten salt flows through the middle channel layer shown in red, in a counter-flow configuration. Inlet/outlet conditions and fixed mass flow rate have been implemented at the fluid inlets. The molten salt has been considered as an incompressible fluid and the fluid solver has been modified accordingly to solve the flow field in the middle channel. However, the flow in the two SCO₂ layers is solved via a compressible solver as discussed in the previous section. Adiabatic conditions have been implemented on the sidewalls. The heat flux is set to be continuous across the fluid/solid interface.

The initial temperature and total mass flow rate for SCO₂ from both channels for different cases are outlined in Table 3. The pressure of SCO₂ and molten salt at the channel inlets have been set to 20 MPa, and 0.35 MPa, respectively. The inlet temperature of the molten salt for all computational cases is identical and equal to 720°C. To meet the one MW/m³ power density design target, the mass flow rate and velocity of the molten salt at the inlet of the hot channel is calculated by assuming 5 KW of heat removal from the molten salt to change its temperature from 720°C to 575°C for all cases outlined in Table 3. Based on these calculations, the mass flow rate and velocity of the molten salt employed in the simulations are

0.029 kg/s and 2 m/s, respectively. The grid independency tests were performed for medium, coarse, and fine mesh corresponding to 980,000, 850,000, and 1,150,000 cells, respectively. The maximum percent error in velocity and pressure within one channel with respect to the medium mesh was less than 8% and 10% for the coarse and fine mesh, respectively. The medium mesh was used in this study as a compromise between computational costs and accuracy. Ten viscous sublayers with a growth factor of 1.1 are implemented close to the wall. The size of the cells near the walls satisfies the requirement of $y^+ \sim 1$, where y^+ is the dimensionless wall distance defined as $y^+ = \frac{y\sqrt{\rho\tau_w}}{\mu}$, where τ_w is the shear stress on the wall, y is the distance from the wall, ρ and μ are the fluid density and viscosity, respectively.

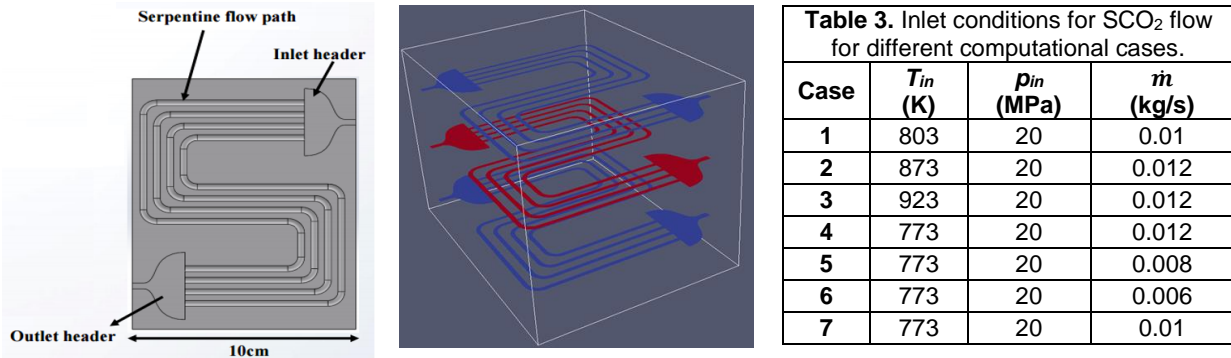


Figure 3. Serpentine ceramic HEX model including three layers of four semi-circular millimeter-channels inside the rectangular block made of the cermet. SCO₂ and molten salt are introduced through the two blue and red layers, respectively.

RESULTS AND DISCUSSION

One of the key elements in designing the ceramic heat exchanger is determining the pressure-drop for the cycle operating conditions. The existence of separated flow at the header and channel bends affects the pressure drop within the HEX and the cycle efficiency. The design criteria are to achieve power density greater than one MW/m³ and pressure drop less than 100 kPa. The sensitivity of the pressure drop, heat transfer effectiveness, and power density to the initial conditions and the optimum conditions on the cold side of the HEX will be discussed. The choice of molten salt on the hot side of the HEX and its effect on the heat transfer effectiveness and power density will be shown. FLiBe, FLiNaK, FLiNaBe, and KCl-MgCl₂ are chosen; firstly, due to their higher applicable temperature compared to Hitec and solar salt for high temperatures >750°C, and secondly, due to their highest thermal conductivity and heat capacity.

The pressure drop within SCO₂ side versus the total SCO₂ mass flow rate with an inlet temperature of 773K is demonstrated in Figure 4. The mass flow rate, pressure, and the inlet temperature of the molten salt is identical and equal to 720°C for all cases. The total pressure drop, including the pressure drop in the headers and channels, rises as the mass flow rate increases. Since the pressure drop on the cold-side of the HEX did not vary significantly with the choice of molten salt for a constant SCO₂ mass flow rate, the average pressure drop for all cases have been shown in this plot. Despite flow recirculation in the headers (Figure 4, right), the total pressure drop satisfies the design condition of 100 kPa. On the same plot, the pressure drop on the hot side of the HEX with different molten salt is shown. The average pressure drop on the hot side was not greatly affected by the change in the mass flow rate on the cold-side. Thus, we reported the average pressure drop on the hot side of the HEX. The maximum pressure drop on the molten salt-side of the HEX does not exceed 33 kPa that is well below the design condition.

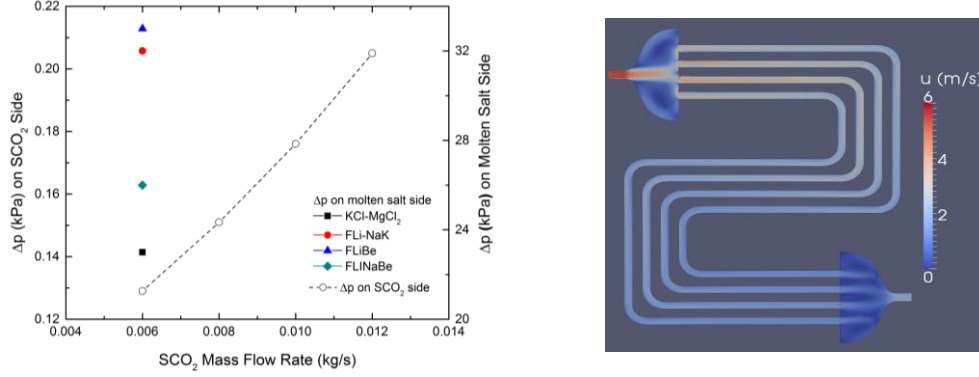


Figure 4. (Left) pressure drop on the cold and hot side of the HEX vs. the total SCO_2 mass flow rate at a constant SCO_2 inlet temperature equal to 773K, (right) contours of velocity magnitude in the cold channel indicating recirculating regions in the header at the inlet.

The HEX effectiveness is defined as $\varepsilon = \frac{C_{hot}(T_{hot,in} - T_{hot,out})}{C_{min}(T_{hot,in} - T_{cold,in})}$ where $T_{hot,in}$ and $T_{hot,out}$ are the bulk temperature, i.e. the mass-weighted average of the temperature at the inlet and outlet of the high-temperature flow channel, respectively defined as $T_i = \frac{\iint \rho_i T_i^* u dA}{\iint \rho_i u dA}$ where ρ , T_i^* , u , and dA are the density, temperature at each location, normal velocity, and cross-sectional surface area, respectively. The index i refers to the inlet or outlet and hot and cold side of the HEX. $C = c_p \dot{m}$ is the heat capacity of the high-temperature flow and $C_{min} = \min\{C_{hot}, C_{cold}\}$. Figure 5 (a) demonstrates the heat transfer effectiveness versus different SCO_2 inlet temperatures for different molten salts. The effectiveness decreases with increasing the inlet temperature of SCO_2 except for $T_{inlet} = 800$ K at which there is a slight increase in the heat transfer effectiveness. The maximum heat transfer effectiveness for FLi-Be, KCl-MgCL₂, and FLi-NaK occurs at 800 K. FLiBe yields the maximum heat transfer effectiveness and FLiNaBe ranks second. Figure 5 (b) demonstrates the heat transfer effectiveness versus SCO_2 mass flow rate at a constant inlet temperature of 773 K. By decreasing the mass flow rate of SCO_2 with a constant inlet temperature of 773 K, heat transfer effectiveness increases. Thus, for the intended range of molten salt inlet and outlet temperature, the maximum heat transfer performance is obtained at 773 K and 0.006 kg/s. KCl-MgCl₂ predicts the lowest heat transfer effectiveness at all conditions. FLi-Be and FLiNaBe yield the highest heat transfer effectiveness. FLiNaBe yields higher heat transfer effectiveness than that of FLiNaK at lower mass flow rates; however, no significant difference was observed between these two salts at higher mass flow rates of SCO_2 .

The HEX is designed to meet the one MW/m^3 power density target. The power density is defined as $\dot{Q} = \frac{C_{hot}}{V} (T_{hot,in} - T_{hot,out})$, where V is the HEX volume. Figure 6 demonstrates the power density versus SCO_2 inlet temperature and mass flow rate for different molten salts. At constant inlet temperature of 773 K, higher mass flow rates lead to higher power densities. The differences between the power densities using different molten salts are not very significant compared to heat transfer effectiveness. By comparing Figure 5 and 6, FLiBe and FLiNaBe are the best candidates for the temperature of interest due to their superior specific heat and conductivity. The predicted power density with FLiBe and FLiNaBe is very close; however, FLiBe provides higher heat transfer effectiveness, especially at lower temperatures compared to that of FLiNaBe. This discrepancy decreases with increasing the inlet temperature of SCO_2 . The optimum SCO_2 temperature and mass flow rate that yield the maximum effectiveness and power density for inlet molten salt temperature of 993 K are outlined in Table 4. Although KCl-MgCl₂ is less expensive than the Fluoride salts, its inferior specific heat and conductivity lowers the heat transfer effectiveness; however, acceptable power density can be obtained at certain SCO_2 initial conditions outlined in Table . It indicates that with SCO_2 inlet temperature of 773 K and molten salt inlet temperature of 993 K, power densities greater than one MW/m^3 and effectiveness greater than 80% are achievable. With the proposed design if the HEX, maximum effectiveness of ~88% is obtained using FLiBe at 993K. In order to achieve the highest effectiveness using KCl-MgCl₂, a more rigorous HEX design is required to increase the surface

area through optimizing the header design and channel patterns, and channel size. This step is currently under investigation and the results will be reported in a future publication.

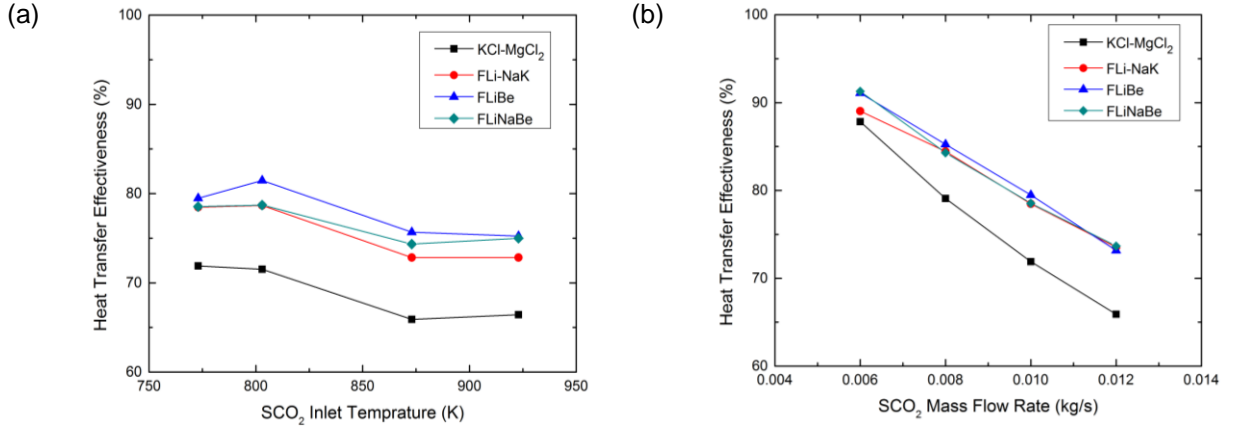


Figure 5. Heat transfer effectiveness for different molten salts vs. (a) SCO₂ inlet temperature for SCO₂ mass flow rate equal to 0.01 kg/s, (b) SCO₂ mass flow rate at a SCO₂ inlet temperature equal to 773K.

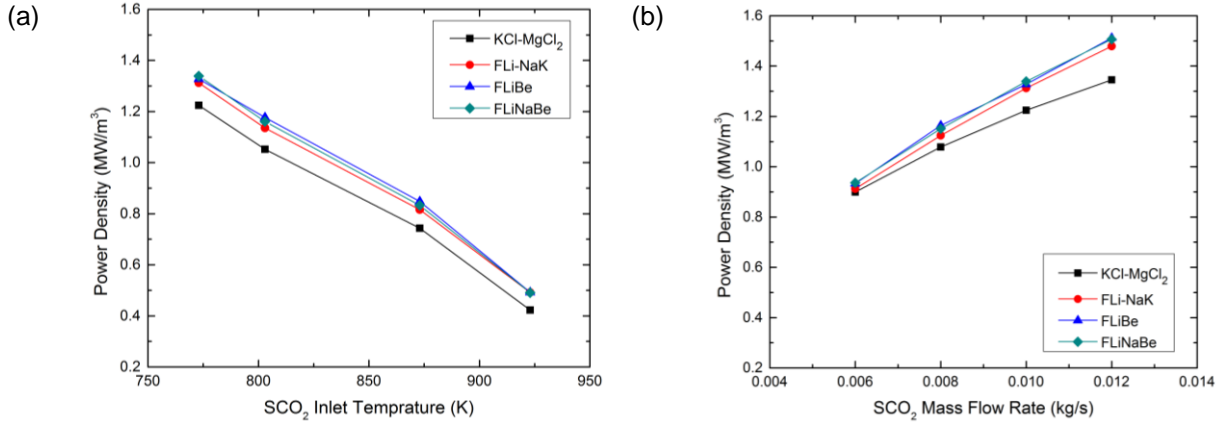


Figure 6. The power density for different molten salts vs. (a) inlet temperature of SCO₂ with a constant SCO₂ mass flow rate equal to 0.001 kg/s, (b) total SCO₂ mass flow rate at constant SCO₂ inlet temperature of 773 K.

The overall heat transfer coefficient is defined as $U = \frac{Q\dot{V}}{A_{ht}\Delta T_m}$ where A_{ht} is the heat transfer area and ΔT_m is the log mean temperature difference defined as $\Delta T_m = \frac{(T_{hot,in}-T_{cold,out})-(T_{hot,in}-T_{cold,in})}{\ln\left(\frac{T_{hot,in}-T_{cold,out}}{T_{hot,out}-T_{cold,in}}\right)}$. T is

the bulk temperature as specified before in this section. The overall heat transfer coefficient versus SCO₂ inlet temperature and mass flow rate are plotted in Figure 7 for different molten salts. As Figure 7 (a) shows, the overall heat transfer coefficient is higher using FLiBe at lower temperatures and decreases with an increase in inlet temperature. The discrepancies between FLiNaBe and FLiNaK is negligible. The overall heat transfer coefficient increases with SCO₂ mass flow rate for all molten salts. Maximum overall heat transfer coefficient occurs with FLiBe, FLiNaBe, and FLiNaK as Figure 7 (b) indicates. The lowest heat transfer coefficient is corresponding to KCl-MgCl₂. There is not a significant difference between FLiNaBe and FLiNaK, especially at lower SCO₂ mass flow rates.

Molten Salt ($T_{in}=993$ K)	SCO ₂ Inlet Temp. (K)	SCO ₂ Mass Flow Rate (kg/s)	Effectiveness (%)	Power Density (MW/m ³)
KCl-MgCl ₂	773	0.008	79.9	1.107
FLi-NaK	773	0.007	86.7	1.106
FLiBe	773	0.007	88.1	1.048
FLiNaBe	773	0.007	87.9	1.043

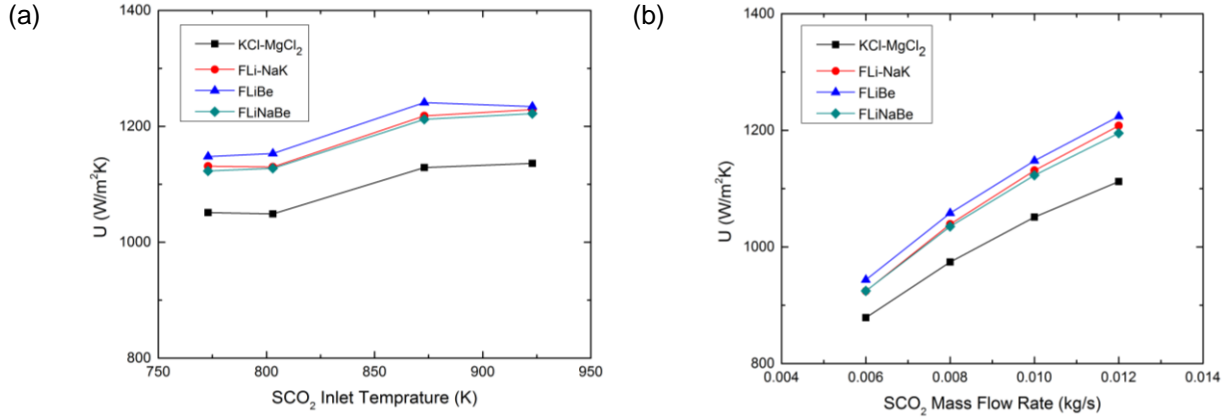


Figure 7. Overall heat transfer coefficient (a) vs. SCO₂ inlet temperature (b) versus SCO₂ mass flow rate for different molten salts on the hot side of the ceramic HEX.

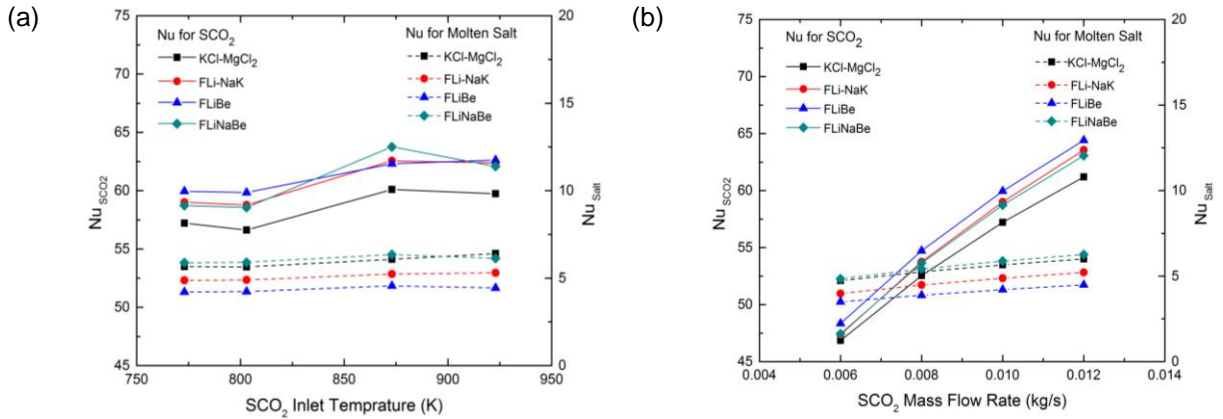


Figure 8. (a) Nusselt number vs. (a) SCO₂ inlet temperature with a SCO₂ mass flow rate equal to 0.001 kg/s, (b) SCO₂ mass flow with SCO₂ inlet temperature equal to 773 K for different molten salts on the hot side of the ceramic HEX.

The Nusselt number versus SCO₂ inlet temperature and SCO₂ mass flow rate for both the hot and cold sides of the ceramic HEX for different choices of molten salt is shown in Figure 8. Nusselt number is defined as $Nu = \frac{UD_h}{k}$ where U is the overall heat transfer coefficient, D_h is the hydraulic diameter of the channels and k is the fluid conductivity. The Nusselt number on the cold side of the ceramic HEX is greater using FLiBe on the hot side. Maximum and minimum Nusselt number on the cold side of the HEX shown in Figure 8 (b) occurs using FLiBe and KCl-MgCl₂ for all tested SCO₂ mass flow rates, respectively. The

Nusselt number on the hot side of the ceramic HEX also increases with mass flow rate. The Nusselt number on the hot side is greater using FLiNaBe due to its larger specific heat compared to KCl-MgCl₂ and FLiNaK and smaller conductivity than FLiBe and FLiNaK. However, the conductivity of FLiNaBe is very close to that of KCl-MgCl₂.

CONCLUSIONS

Department of Energy (DOE) Sunshot objective for clean and affordable energy conversion is to approach 6¢/kWh electricity cost by 2020. Increasing the cycle efficiency from ~35% to ~50% for electrical energy conversion in concentrated solar power (CSP) systems requires operation of HEXs at temperatures greater than 750°C. The primary HEX is responsible for heat transfer between high-temperature (>750°C) molten salts as the heat transfer medium and SCO₂ as the working fluid in the SCO₂ Brayton cycle as the power block of CSP plants. A novel HEX made of a special metal-coated composite (cermet) developed at Purdue University capable of withstanding temperatures greater than 750°C is designed in this paper. Computational models are deployed to demonstrate the capabilities and optimum initial conditions of the designed ceramic HEX to meet one MW/m³ power density and pressure drop less than 100 kPa. A multi-region computational model implemented in open source computational fluid dynamics (CFD) code OpenFOAM is used to study the thermal-hydraulic behaviors of SCO₂ and molten salt inside the channels and conjugate heat transfer between the solid and fluid regions of the HEX. The computational model was compared with the available experimental measurements of a ceramic HEX with nine semi-circular channels made of stainless steel (SS316).

The HEX model is comprised of three layers of semi-circular channels and internal headers for distribution of SCO₂ and molten salt flow into the channels made of the special cermet. Heat transfer effectiveness, overall heat transfer coefficient, power density, and pressure drop were calculated for seven different initial conditions for SCO₂ and various molten salts, including FLiBe, FLiNaBe, FLiNaK, and KCl-MgCl₂. Optimum design conditions that met the design criteria were obtained. With SCO₂ inlet temperature of 773 K and molten salt inlet temperature of 993 K, power densities greater than one MW/m³ and effectiveness greater than 80% were achievable. With the proposed design of the ceramic HEX, maximum effectiveness of ~88% is obtained using FLiBe at 993K. To achieve the highest effectiveness using KCl-MgCl₂, a more rigorous HEX design is required to increase the surface area through optimizing the header design and channel patterns, or channel size in future studies. It is expected that by reducing the channel size and increasing the number of channels much higher effectiveness will be achieved while keeping the pressure drop within the acceptable limit. The overall heat transfer coefficient increased with SCO₂ mass flow rate for all molten salts. Maximum and minimum overall heat transfer coefficient occurred with FLiBe and KCl-MgCl₂, respectively. No significant difference between FLiNaBe and FLiNaK was observed, especially at lower SCO₂ mass flow rates.

REFERENCES

1. Dostal, V., M.J. Driscoll, and P. Hejzlar, *A supercritical carbon dioxide cycle for next generation nuclear reactors*. 2004, MIT-ANP-TR-100.
2. Dostal, V., et al. *A supercritical CO₂ gas turbine power cycle for next-generation nuclear reactors*. in *10th International Conference on Nuclear Engineering*. 2002. American Society of Mechanical Engineers.
3. Dostal, V., P. Hejzlar, and M.J. Driscoll, *The supercritical carbon dioxide power cycle: comparison to other advanced power cycles*. Nuclear technology, 2006. **154**(3): p. 283-301.
4. Ahn, Y., et al., *Review of supercritical CO₂ power cycle technology and current status of research and development*. Nuclear Engineering and Technology, 2015. **47**(6): p. 647-661.
5. Kulhánek, M. and V. Dostal. *Thermodynamic analysis and comparison of supercritical carbon dioxide cycles*. in *Proceedings of Supercritical CO₂ Power Cycle Symposium*. 2011.
6. Moiseyev, A. and J.J. Sienicki, *Investigation of alternative layouts for the supercritical carbon dioxide Brayton cycle for a sodium-cooled fast reactor*. Nuclear Engineering and Design, 2009. **239**(7): p. 1362-1371.
7. Strakey, P., et al., *Technology needs for fossil fuel supercritical CO₂ power systems*. Proceeding of the 4th international symposium supercritical CO₂ power cycles, Pittsburgh, PA, USA, 2014.

8. Yari, M., *A novel cogeneration cycle based on a recompression supercritical carbon dioxide cycle for waste heat recovery in nuclear power plants*. International Journal of Exergy, 2012. **10**(3): p. 346-364.
9. Backstr, V. and P. Erens, *NaK as a primary heat transfer fluid in thermal solar power installations*. 2012.
10. Kotzé, J.P., T.W. von Backström, and P.J. Erens, *NaK as a primary heat transfer fluid in thermal solar power installations*. Proceeding of SolarPaces, 2012: p. 11-14.
11. Turchi, C.S., Z. Ma, and J. Dyreby. *Supercritical CO₂ for application in concentrating solar power systems*. in *SCCO₂ Power Cycle Symposium*, RPI, Troy, NY. 2009.
12. Turchi, C.S., et al. *Thermodynamic study of advanced supercritical carbon dioxide power cycles for high performance concentrating solar power systems*. in *ASME 2012 6th International Conference on Energy Sustainability collocated with the ASME 2012 10th International Conference on Fuel Cell Science, Engineering and Technology*. 2012. American Society of Mechanical Engineers.
13. Turchi, C.S., et al., *Thermodynamic study of advanced supercritical carbon dioxide power cycles for concentrating solar power systems*. Journal of Solar Energy Engineering, 2013. **135**(4): p. 041007.
14. Avila-Marin, A.L., J. Fernandez-Reche, and F.M. Tellez, *Evaluation of the potential of central receiver solar power plants: configuration, optimization and trends*. Applied energy, 2013. **112**: p. 274-288.
15. Ma, Z. and C. Turchi. *Advanced supercritical carbon dioxide power cycle configurations for use in concentrating solar power systems*. in *Proceedings of Supercritical CO₂ Power Cycle Symposium*. 2011.
16. Padilla, R.V., et al., *Exergetic analysis of supercritical CO₂ Brayton cycles integrated with solar central receivers*. Applied Energy, 2015. **148**: p. 348-365.
17. Al-Sulaiman, F.A. and M. Atif, *Performance comparison of different supercritical carbon dioxide Brayton cycles integrated with a solar power tower*. Energy, 2015. **82**: p. 61-71.
18. Behar, O., A. Khellaf, and K. Mohammedi, *A review of studies on central receiver solar thermal power plants*. Renewable and sustainable energy reviews, 2013. **23**: p. 12-39.
19. Wang, K. and Y.-L. He, *Thermodynamic analysis and optimization of a molten salt solar power tower integrated with a recompression supercritical CO₂ Brayton cycle based on integrated modeling*. Energy Conversion and Management, 2017. **135**: p. 336-350.
20. Oró, E., et al., *Thermal Energy Storage Implementation Using Phase Change Materials for Solar Cooling and Refrigeration Applications*. Energy Procedia, 2012. **30**: p. 947-956.
21. Neises, T.W. and C.S. Turchi. *Supercritical CO₂ Power Cycles: Design Considerations for Concentrating Solar Power*. in *4th International Symposium—Supercritical CO₂ Power Cycles*, Pittsburgh, PA, Sept. 2014. Citeseer.
22. Lipke, D.W., et al., *Near net-shape/net-dimension ZrC/W-based composites with complex geometries via rapid prototyping and displacive compensation of porosity*. Journal of the European Ceramic Society, 2010. **30**(11): p. 2265-2277.
23. Song, G.-M., Y.-J. Wang, and Y. Zhou, *The mechanical and thermophysical properties of ZrC/W composites at elevated temperature*. Materials Science and Engineering: A, 2002. **334**(1): p. 223-232.
24. Sabharwall, P., et al., *Molten salts for high temperature reactors: University of Wisconsin molten salt corrosion and flow loop experiments—Issues identified and path forward*. Idaho National Laboratory Report INL/EXT-10-18090, 2010.
25. Anderson, N. and P. Sabharwall, *Molten Salt Mixture Properties (KF-ZrF₄ and KCl-MgCl₂) for Use in RELAP5-3D for High-Temperature Reactor Application*. Nuclear technology, 2012. **178**(3): p. 335-340.
26. Serrano-López, R., J. Fradera, and S. Cuesta-López, *Molten salts database for energy applications*. Chemical Engineering and Processing: Process Intensification, 2013. **73**: p. 87-102.
27. Sohal, M.S., et al., *Engineering database of liquid salt thermophysical and thermochemical properties*. Idaho National Laboratory, Idaho Falls, 2010.
28. Delpech, S., et al., *Molten fluorides for nuclear applications*. Materials Today, 2010. **13**(12): p. 34-41.
29. Heatric, P., *PCHE applications*. 2004.

30. Jarrahbashi, D., S.R. Pidaparti, and D. Ranjan, *Nucleation of super-critical carbon dioxide in a venturi nozzle*. Nuclear Engineering and Design, 2016. **310**: p. 69-82.
31. Yuan, H., et al., *Numerical modeling of supercritical carbon dioxide flow in see-through labyrinth seals*. Nuclear Engineering and Design, 2015. **293**: p. 436-446.
32. Kruizenga, A., et al., *Heat Transfer of Supercritical Carbon Dioxide in Printed Circuit HEX Geometries*. Journal of Thermal Science and Engineering Applications, 2011. **3**(3): p. 031002-031002-8.
33. Jasak, H, *OpenFOAM: Open source CFD in research and industry*, International Journal of Naval Architecture and Ocean Engineering, 2009. **1**(2): 89-94.

ACKNOWLEDGEMENTS

The support from the Department of Energy-EERE under award number DE-EE0007117 is greatly appreciated.